



## Research article

# Graphene oxide doping in tropical almond (*terminalia catappa* L.) fruits extract mediated green synthesis of TiO<sub>2</sub> nanoparticles for improved DSSC power conversion efficiency

Nofrijon Sofyan<sup>a,d,\*</sup>, Alry Mochtar Jamil<sup>a</sup>, Aga Ridhova<sup>b</sup>,  
Akhmad Herman Yuwono<sup>a,d</sup>, Donanta Dhaneswara<sup>a,d</sup>, Jeffrey W. Fergus<sup>c</sup>

<sup>a</sup> Department of Metallurgical and Materials Engineering, Faculty of Engineering, Universitas Indonesia, Depok 16424 Indonesia

<sup>b</sup> Research Center for Metallurgy, National Research and Innovation Agency, Tangerang Selatan, Banten 15314, Indonesia

<sup>c</sup> Materials Research and Education Center, Auburn University, Auburn, AL 36849, USA

<sup>d</sup> Advanced Materials Research Center, Faculty of Engineering, Universitas Indonesia, Depok 16424 Indonesia

## ARTICLE INFO

## Keywords:

Dye sensitized-solar cells (DSSC)  
Graphene oxide (GO)  
Green synthesis  
Power conversion efficiency (PCE)  
Titanium dioxide (TiO<sub>2</sub>)  
Tropical almond

## ABSTRACT

The power conversion efficiency (PCE) of a dye-sensitized solar cell (DSSC) device depends on its semiconductor characteristics. Titanium dioxide (TiO<sub>2</sub>) nanoparticles are a semiconductor material commonly used in the DSSC device whose characteristics depend on the synthesis process. There are many routes to synthesize TiO<sub>2</sub>, however, they typically involve hazardous approaches, which may cause risk to the environment. Green synthesis is an environmentally friendly alternative method using ecological solvents that eliminates toxic waste and reduces energy consumption. In this work, tropical almond (*Terminalia catappa* L.) was used as a natural capping agent in the green synthesis to control the growth of TiO<sub>2</sub>. In addition, graphene oxide (GO) was used as a dopant to increase the performance of DSSC device. The results are convincing, in which the addition of 0.0017 % GO doping in tropical almond extract mediated green synthesis of TiO<sub>2</sub> improved the PCE from 0.85 % to 1.72 %. These results suggest that GO-modified TiO<sub>2</sub> nanoparticles green synthesized using tropical almond extract have great potential in the fabrication of DSSC devices with good PCE, low cost, and low environmental impact.

## 1. Introduction

With the decreasing sources of energy derived from fossil-based fuels, the search for alternative energy, both from new and renewable energy sources, continues to be carried out by many investigators. Solar energy has attracted a lot of interest, since sunlight, especially in tropical countries, is abundant and constant throughout the year [1]. In its development, to harvest the energy from the sun, several solar cell devices have been developed by many researchers, including silicon-based [2–4], thin-film [5], dye-sensitized [6], and perovskite solar cells [7]. Each device has its own advantages and disadvantages in terms of ease of fabrication, cost of processing technology, and environmentally friendliness.

The dye sensitized solar cell (DSSC) is the 3rd generation solar cell that is considered as an environmentally friendly renewable

\* Corresponding author. Department of Metallurgical and Materials Engineering, Faculty of Engineering, Universitas Indonesia, Depok 16424 Indonesia.

E-mail address: [nofrijon.sofyan@ui.ac.id](mailto:nofrijon.sofyan@ui.ac.id) (N. Sofyan).

<https://doi.org/10.1016/j.heliyon.2024.e29370>

Received 1 February 2024; Received in revised form 11 March 2024; Accepted 7 April 2024

Available online 9 April 2024

2405-8440/© 2024 The Author(s). Published by Elsevier Ltd. This is an open access article under the CC BY-NC license (<http://creativecommons.org/licenses/by-nc/4.0/>).

## Nomenclature

C	capacitor
c	speed of light
$E_g$	bandgap energy
eV	electron Volt
h	Planck's constant
s	second
p	probability
R	resistor

### Greek symbols

$\Omega$	Ohm (the unit of electrical resistance)
$\alpha$	absorption coefficient (optical bandgap), significance level (statistics)
$\gamma$	electron transition
$\lambda$	wavelength
$\nu$	frequency

### Abbreviations

ANOVA	analysis of variance
DSSC	dye-sensitized solar cell
DRS	diffuse reflectance
EDX	energy dispersive X-ray spectroscopy
EIS	electrochemical impedance spectroscopy
FESEM	field emission scanning electron microscopy
FTIR	Fourier-transform infrared spectroscopy
FTO	fluorine-doped tin oxide
FWHM	full width at half maximum
GO	graphene oxide
HOMO	highest occupied molecular orbital
HRTEM	high resolution transmission electron microscopy
LUMO	lowest unoccupied molecular orbital
PCE	power conversion efficiency
SAED	selected area diffraction
TiO <sub>2</sub>	titanium dioxide
TEM	transmission electron microscopy
TBA	tetrabutylammonium
TTIP	titanium tetraisopropoxide
UV-Vis	ultraviolet visible
XRD	X-ray diffraction

### Subscripts

oc	open circuit
sc	short circuit
g	gap

energy alternative [8]. The main problem currently being faced by the DSSC is its low current density and power conversion efficiency (PCE) [9]. Many efforts have been performed to improve DSSC performance, for example through processing or manipulating semiconductor materials and their structure [10]. One important characteristic of semiconductors is crystallite size, which affects electron transport properties within the semiconductor [11,12]. Furthermore, device performance can be improved via dopant addition, which improves the electron transport properties [13]. For example, doping with graphene oxide can improve electron transfer properties in DSSC [14]. The increase in PCE because of dopant addition and crystallite size manipulation are due to increasing the electron transport, controlling the rate of recombination reactions, and or decreasing the band gap energy [15,16]. Structural manipulation methods through size reduction and graphene oxide addition, however, are not without their respective difficulties [17]. For example, the addition of excess graphene concentration will affect light absorption, and over time graphene particles can create a barrier to the electron transfer process that leads to gradual degradation in the open-circuit voltage ( $V_{oc}$ ) and short-circuit current ( $I_{sc}$ ) [18–20]. In addition, the complicated and high-temperatures processes for semiconductor fabrication create difficulties [21], and thus further research on the improvement of DSSC performance is still needed.

Titanium dioxide (TiO<sub>2</sub>) nanoparticles are a semiconductor material commonly used in the DSSC device whose characteristics depend on the synthesis process. There are many routes to synthesize titanium dioxide (TiO<sub>2</sub>) nanoparticles, including chemical and

**Table 1**  
Sample coding and composition (v/v).

Graphene Oxide	Tropical Almond		
	0.00 %	0.60 %	0.80 %
0.0000 %	1A	1B	1C
0.0017 %	2A	2B	2C
0.1600 %	3A	3B	3C

Control: TiO<sub>2</sub> nanoparticle P25 Degussa.

physical methods [22]. The main problem with the chemical or physical processes is that chemical or physical hazards may cause risk to the environment [23]. Many researchers have been focusing on reducing this drawback by using a green approach towards the synthesis of metal-oxide nanoparticles [24,25]. This green synthesis approach ensures that the degree of environmental friendliness that is crucial for future world sustainability will be maintained [4]. Several natural resources have been used for the green synthesis of TiO<sub>2</sub>, for examples *Citrus limon* [26], *Bixa orellana* [27], *Terminalia catappa* and *Carissa carandas* [28]. The one from *Terminalia catappa* and *Carissa carandas* has not been used for DSSC applications.

In this work, combination of the two processes, namely the use of tropical almond extract as a medium and graphene oxide (GO) as a dopant in the green synthesis of TiO<sub>2</sub> on the improved efficiency of a DSSC solar cell were carried out. Tropical almond (*Terminalia catappa* L.) is a large tropical tree with vast natural distribution and one of the most common trees across Southeast Asia [29]. This tree is widely grown as an ornamental tree for its deep shade. Its ripe fruit has a reddish color with a seed that is edible, raw or cooked, and is the origin of the almond common names, although the seed is much smaller size than a real almond. Most of the time, the fruits are abandoned and become waste in the environment. If this fruit can be utilized, then one solution to the waste can be overcome and at the same time increasing the added value of the wasted fruit. Chemical constituents contained in the tropical almond fruit are supposed to fulfil at least one of the given functions, according to the classic green chemistry idea: metal salt reduction, hydrolysis of the Ti<sup>4+</sup> precursor, solubilization, and possibly reducing and capping agents in the green synthesis of TiO<sub>2</sub> [30]. Several advantages of using this tropical almond fruit include being easy to obtain, easy to extract, and economical.

There are two objectives of this work. The first is to confirm the characteristics of TiO<sub>2</sub> nanoparticles green synthesized using tropical almond fruit as a natural capping agent performed by Rajendhiran et al. [28] and use it in the DSSC device. The second is to examine the improvement of electron transfer characteristics of the green synthesized TiO<sub>2</sub> in the DSSC device by using graphene oxide (GO) as a dopant.

## 2. Experimental methods

For reproducibility and statistical analysis, the experiment was repeated twice with similar results. In the first run, there was no replicate, but for the second run, the experiment was run in duplo. The statistical analysis presented here is thus the blend of the first and second runs. Details of the experiments are given in the following sections.

### 2.1. Tropical almond fruits extract preparation

Ripe tropical almond fruits were collected from the trees that grow on the Universitas Indonesia Faculty of Engineering campus. The herbarium voucher number is WAM1045 deposited at the Department of Biology Herbarium, Faculty of Mathematics and Natural Sciences, Universitas Indonesia.

The extraction followed the procedure described by Rajendhiran et al. [28] with slight modification. A total of three intact ripe tropical almond fruits were prepared and washed under running water to remove any dirt and air dried at room temperature. The fruit pericarp was peeled off until the flesh of the mesocarp was visible followed by cutting and slicing the mesocarp in the forms of flakes. The flakes were dried under room condition for 48 h to remove the excess moisture before being crushed into fine powder (80 mesh) using a household blender.

Fifty grams of the fine powders were put in a beaker and 50 ml of distilled water was added until all the powders were submerged. The mixture was heated at 90 °C for 10 min under magnetic stirring and then allowed to cool down to room temperature. The remaining solid powders were removed from the mixture, and the extract was filtered until a red-brown color filtrate was obtained. The filtrate was stored in a dark bottle and ready for further treatment or characterization. The tropical almond images and the obtained extract are given in the [Supplement Fig. S1](#).

### 2.2. Green synthesis of TiO<sub>2</sub>

Precursors for the green synthesis include titanium tetraisopropoxide (Ti [OCH(CH<sub>3</sub>)<sub>2</sub>]<sub>4</sub>, TTIP Sigma-Aldrich 97 %), ethanol (Merck), graphene oxide (GO, ITNANO 99 %), and tropical almond fruit extract obtained from the previous stage. In this work, nine variations of samples plus one from the commercial TiO<sub>2</sub> P25 as a comparison were prepared. Sample coding and compositions are given in [Table 1](#).

All precursors were prepared following the sol-gel method because of its versatility and easiness [31]. The green synthesis was modified from the work of Rajendhiran et al. [28] and is explained as follows. Five ml of TTIP was poured into a beaker glass to which

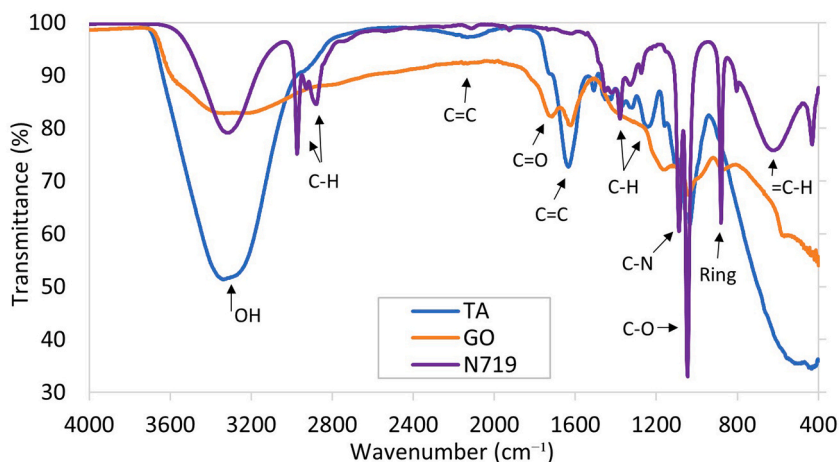


Fig. 1. Infrared spectra of tropical almond extract, commercial graphene oxide (GO), and commercial dye N719.

84 ml of ethanol was added dropwise. In the meantime, GO was dispersed in ethanol with the variation concentrations described in Table 1 and was added into the TTIP solution. These GO concentrations have never been studied before by other researchers. Similar work by Shahid et al. [20] but on the addition of graphene used the concentrations of 0, 0.005, 0.01, 0.015, 0.020 and 0.025 wt%. The mixture was then sonicated in an ultrasonic bath for about 20 min before being placed under a magnetic stirrer for 120 min. Tropical almond extract with various concentrations, also described in Table 1, was added and the stirring was continued for another 80 min. The mixture was allowed to stand for 24 h until a gel forms at the bottom of the container. The solution was removed to obtain the wet gel. The wet gel was dried at 60 °C for 15 min before being calcined at 400 °C for 2 h. The dry powders of synthesized TiO<sub>2</sub> (1A), green synthesized TiO<sub>2</sub> (1B, 1C), GO doped synthesized TiO<sub>2</sub> (2A, 3A), and GO doped green synthesized TiO<sub>2</sub> (2B–3C) nanoparticles were obtained and ready for further treatment and or characterization.

### 2.3. DSSC device fabrication

Two fluorine-doped tin oxide (FTO) conductive glass substrates were prepared and cleaned for each variation in accordance with Table 1. The FTO glass substrate average surface resistance of the conductive side verified using a multimeter was 16 Ω. There were 9 DSSC devices plus one for the control from TiO<sub>2</sub> P25 (Degussa, E-Merck). One of the FTO glass substrates was prepared as an anode. For this anode, 0.1 mg of GO-doped TiO<sub>2</sub> obtained from the green synthesis was added with three drops of ethanol, 0.02 mL acetyl acetate, and two drops of Triton X-100 (Sigma Aldrich) to form colloidal suspension. The colloidal suspension was mixed until homogeneous and deposited on the conductive side of the FTO glass substrate over an area of about 1 cm<sup>2</sup> using the doctor blade method. After deposition, the substrate was calcined at 400 °C for 30 min and allowed to cool down to room temperature. In the meantime, commercial dye solution of 0.8 mM was prepared as a sensitizer by dissolving 0.1 g *cis*-diisothiocyanato-bis(2,2'-bipyridyl-4,4'-dicarboxylato) ruthenium (II) bis(tetrabutylammonium), a commercial ruthenizer 535-bis TBA, also known as N719 (C<sub>58</sub>H<sub>86</sub>O<sub>8</sub>N<sub>8</sub>S<sub>2</sub>Ru, Solaronix) in 100 ml ethanol [32]. The structure of this sensitizer is given in the Supplement Fig. S2. The already calcined anode was immersed in the sensitizer dye solution for 24 h.

The other FTO glass substrate was prepared as a counter electrode. At one corner of this counter electrode, a small perforation of about 1 mm was carefully drilled using a glass drill bit. After perforation, on the FTO conductive side, platinum paste (Platisol T/SP, Solaronix) was deposited using the same method applied for the anode. Finally, the two electrodes were joined together using silicon rubber sealant separated by an interface to avoid any short circuit and were cured for 24 h. After 24 h, the electrolyte I<sub>2</sub>/I<sub>3</sub><sup>-</sup> (Iodolyte Z-50, Solaronix) was injected carefully through the small perforation on the counter electrode side until the whole volume was filled. Once the electrolyte had been injected, the hole was sealed, and the device was ready for the performance examination. The schematic of this device fabrication is given in the Supplement Fig. S3.

### 2.4. Characterization

All characterizations were performed at room temperature and ambient condition with no control over pressure nor humidity except as otherwise stated. The characteristics of the obtained materials were observed using infrared spectroscopy (FTIR, PerkinElmer ATR Spectrum One) for functional groups identification, ultraviolet visible diffuse reflectance spectroscopy (UV-Vis DRS, Shimadzu UV2450) for reflectance characteristic, X-ray diffraction (XRD, ARL OPTX-2050) for crystallographic information, Raman spectroscopy (Raman iHR320 HORIBA) for detailed information on chemical structure and phase information, field emission scanning electron microscope equipped with energy dispersive X-ray spectroscopy (FESEM/EDX, FEI Inspect F50) for surface morphology and composition, and transmission electron microscope (TEM, FEI Tecnai G2 20 S-Twin) for high-resolution imaging and selected area diffraction. The electrochemical activities were recorded and characterized using electrochemical impedance spectroscopy (EIS, ZIVE

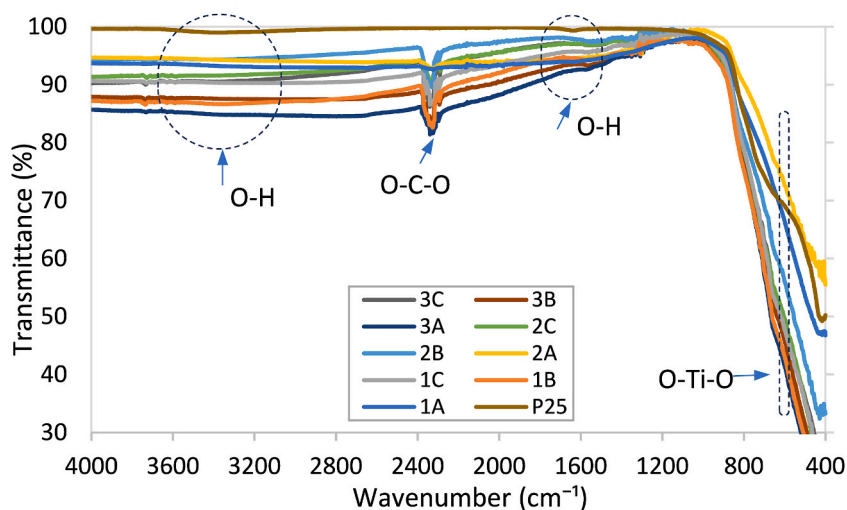


Fig. 2. Infrared spectra of TiO<sub>2</sub> obtained from the green synthesis with sample variations 1A-3C and from the commercial TiO<sub>2</sub> P25.

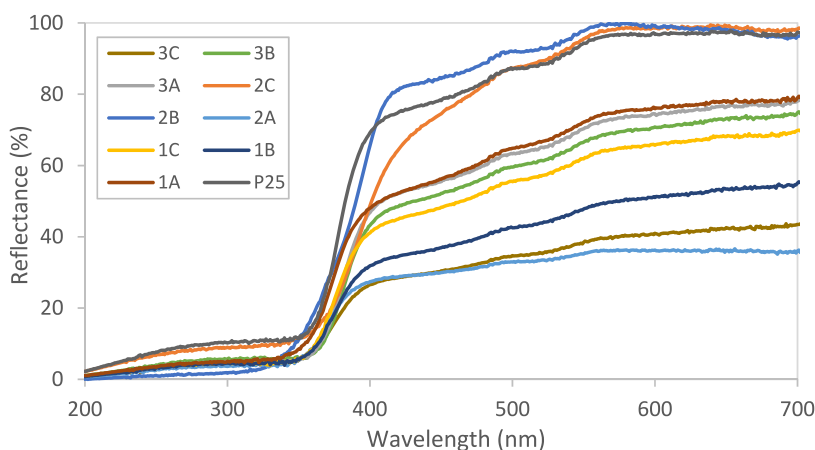


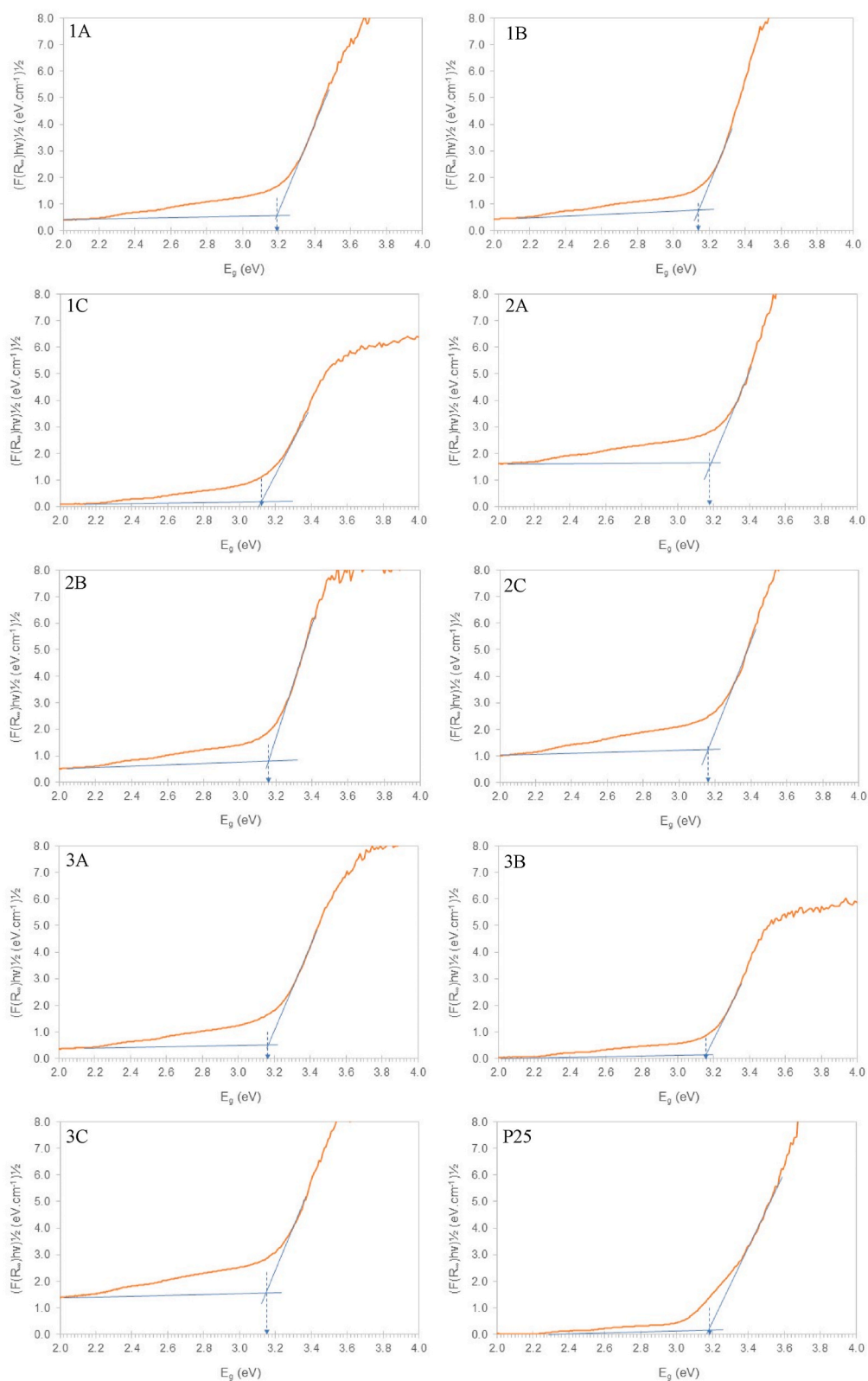
Fig. 3. UV-Vis DRS spectra of TiO<sub>2</sub> obtained from the green synthesis with sample variations 1A-3C and from the commercial TiO<sub>2</sub> P25.

5 WonATech) under room light condition, whereas the photovoltaic activities were examined using a source meter (Keithley 2450) interfaced with a solar simulator (ABET Sunlite™) under a standard illumination of 1000 W/m<sup>2</sup>. When needed, analysis of variance (ANOVA) using MatLAB® was employed to statistically analyze the difference between the treatments at confidence level 90 % ( $\alpha = 0.1$ ).

### 3. Results and discussion

#### 3.1. Infrared characteristics

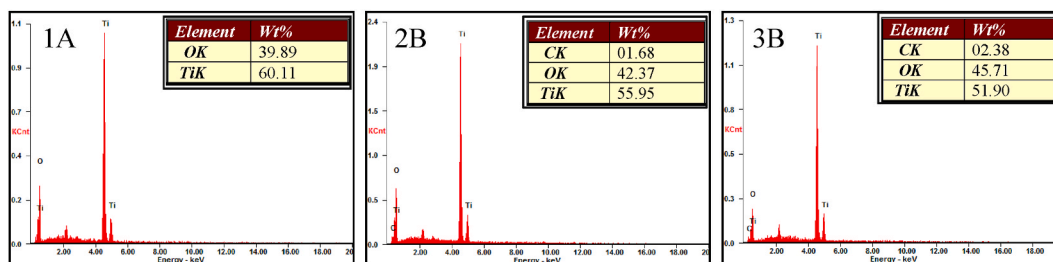
After the extraction, the functional groups of the tropical almond extract along with GO and commercial dye N719 were examined using infrared spectroscopy. Fig. 1 shows the infrared spectra of tropical almond extract, commercial GO, and commercial dye N719. The spectrum of tropical almond extract shows several absorption bands. The absorption band at 3405.47 cm<sup>-1</sup> indicates the presence of O-H group with a very strong and broad signal, the type of phenol compound. The absorption band at 1570.12 cm<sup>-1</sup> is a form of C=C group with the ring of aromatic compound. The absorption band at 1417.74 cm<sup>-1</sup> corresponds to C-H stretching with the type of alkane compound. The absorption bands at 1069.57–1181.45 cm<sup>-1</sup> form C-O stretching with medium weak intensity typical of alcohol compound. The absorption bands at 751.31–872.83 cm<sup>-1</sup> are the form of C=C bending with the type of alkene compound. The peaks belonging to the vibration of 3366 cm<sup>-1</sup>, 1650 cm<sup>-1</sup> and 679 cm<sup>-1</sup> in the spectra correspond to the characteristic peaks of flavonoids. The presence of these functional groups has also been found by others [28,33], which could be an indication of the presence of quercetin and related compounds known as flavonoids compound. Other investigators obtained that the yellow colors in the extract are



**Fig. 4.** Tauc plot for determining the bandgap energy of  $\text{TiO}_2$  obtained from the green synthesis with sample variations 1A-3C and from the commercial  $\text{TiO}_2$  P25.

**Table 2**Bandgap energy (eV) of TiO<sub>2</sub> with sample variations. Standard errors are given in the parenthesis.

Graphene Oxide	Tropical Almond		
	0.00 %	0.60 %	0.80 %
0.0000 %	3.19 (0.01)	3.14 (0.02)	3.12 (0.05)
0.0017 %	3.18 (0.02)	3.16 (0.00)	3.16 (0.01)
0.1600 %	3.16 (0.01)	3.15 (0.01)	3.15 (0.01)

TiO<sub>2</sub> P25 = 3.19(0.01).**Fig. 5.** Energy dispersive X-ray spectra of synthesized TiO<sub>2</sub> represented by sample 1A, 2B, and 3B. Elemental compositions are given in the inset.

due to hydroxy and methoxy derivatives of flavones and isoflavones [34,35] and are believed to have the influence on the crystal growth of TiO<sub>2</sub> semiconductors during the green synthesis [36]. Further work, however, is yet to be carried out to confirm this proposition.

The spectrum of commercial GO also shows several absorption bands revealing various oxygen configurations in the structure including the vibration modes of epoxide (C–O–C) (1230–1320 cm<sup>-1</sup>), sp<sup>2</sup>-hybridized C=C (1500–1600 cm<sup>-1</sup>, in-plane vibrations), carboxyl (COOH) (1650–1750 cm<sup>-1</sup> including C–OH vibrations at 3530 and 1080 cm<sup>-1</sup>), ketonic species (C=O) (1600–1650 cm<sup>-1</sup>, 1750–1850 cm<sup>-1</sup>) and hydroxyl (namely phenol, C–OH) (3050–3800 cm<sup>-1</sup> and 1070 cm<sup>-1</sup>) with all C–OH vibrations from COOH and H<sub>2</sub>O [37–39].

For the commercial dye N719, the spectrum shows absorption bands at 3000–3600 and 2500–3000 cm<sup>-1</sup> regions, corresponding to the presence of the –OH and C–H groups, respectively [40]. Other absorption bands of thiocyanate (NCS), carbonyl (C=O), bipyridine (C=C), tetrabutylammonium (TBA), and carboxylic acid and carboxylate groups (C–O) can be observed at 2100, 1710, 1542, 1464, and 1256 cm<sup>-1</sup>, respectively [41]. More pronounced peaks of C–N, C–O, aromatic para ring, and =C–H are observed at 1087, 1046, 880, and 623 cm<sup>-1</sup>, respectively [42].

The infrared spectra of TiO<sub>2</sub> obtained from the green synthesis prepared at different tropical almond concentration and GO plus the one from commercial TiO<sub>2</sub> P25 as a comparison were also collected to observe any change of functional groups during the synthesis. As can be seen from the spectra given in Fig. 2, the spectrum of commercial TiO<sub>2</sub> P25 shows weak absorption band at around 3370, 1630 and 650 cm<sup>-1</sup> associated with stretching vibrations of hydrogen-bonded water molecules and hydroxyl groups, bending vibrations of O–H group and Ti–O–Ti bridging stretching mode, respectively [43]. The spectrum of TiO<sub>2</sub> obtained from the synthesis using pure ethanol (1A) shows the same characteristic as that of commercial TiO<sub>2</sub> P25 but at a little lower transmittance. The same are true for the spectra of TiO<sub>2</sub> obtained from the green synthesis prepared at different tropical almond concentration [28] and GO (1B–3C) plus an additional absorption band at 2326 cm<sup>-1</sup> possibly corresponding to the O–C–O linear vibrations from GO doping [44–46].

### 3.2. Optical characteristics

The optical characteristics of TiO<sub>2</sub> obtained from the green synthesis and the one from the commercial TiO<sub>2</sub> P25 were analyzed using UV–Vis DRS. The results in the forms of reflectance spectra with sample variations 1A–3C and commercial TiO<sub>2</sub> P25 are given in Fig. 3. These UV–Vis DRS spectra were further examined to reveal the optical characteristics in the forms of bandgap energy. The bandgap energies from these UV–Vis DRS spectra were calculated using the Kubelka–Munk relation as proposed by Makula et al. [47] and expressed as in Eq. (1),

$$(F(R_{\infty}) \cdot h\nu)^{1/\gamma} = B(h\nu - E_g) \quad (1)$$

where  $h$  is the Planck constant,  $\nu$  is the photon's frequency,  $E_g$  is the band gap energy,  $F(R_{\infty})$  is the Kubelka–Munk function, and  $B$  is a constant. The  $\gamma$  factor depends on the nature of the electron transition and is equal to  $\frac{1}{2}$  or 2 for the direct and indirect transition band gaps, respectively. The Kubelka–Munk function,  $F(R_{\infty})$ , is given by the expression  $F(R_{\infty}) = (1 - R_{\infty})^2 / 2R_{\infty}$ , where  $R_{\infty}$  is the reflectance. In this work, the bandgap energy was calculated by fitting the data in Tauc plot  $(F(R_{\infty}) \cdot hc/\lambda)^{1/2}$  vs  $hc/\lambda$  assuming an indirect allowed transition bandgap energy [47,48] and the results are depicted in Fig. 4. Using this calculation, the bandgap energy for each specimen was obtained and the results are tabulated in Table 2. The bandgap energy reduces with the use of tropical almond medium, agrees

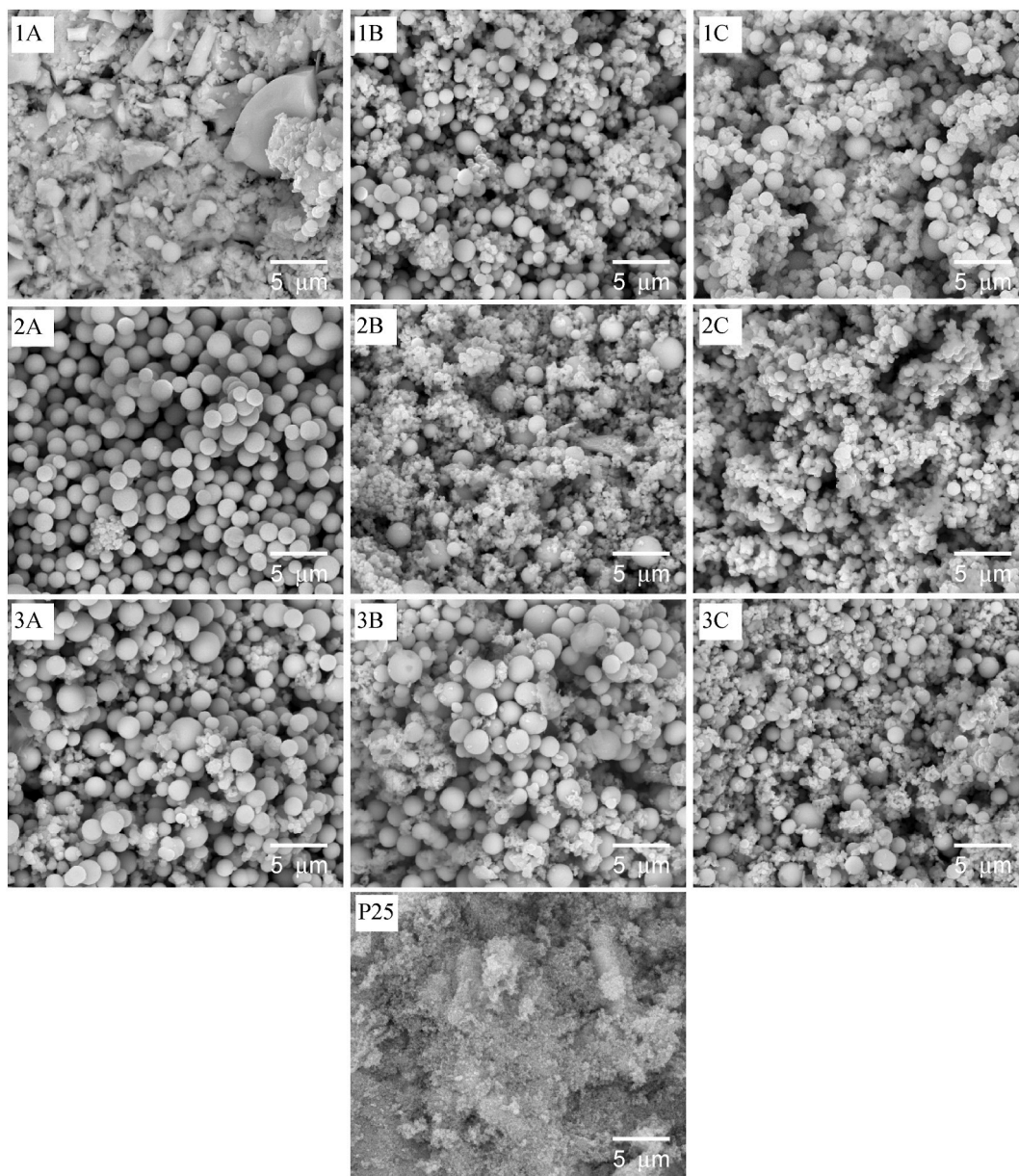


**Fig. 6.** Electron images of  $\text{TiO}_2$  obtained from the green synthesis with sample variations 1A-3C and commercial  $\text{TiO}_2$  P25. The scale bar is  $5 \mu\text{m}$ .

with the previous results [28]. The presence of GO alone also decreases the bandgap energy, agrees with the work of others [20]; however, the presence of GO during the green synthesis increases the bandgap energy before decreasing with more GO concentration. Nevertheless, the two-way ANOVA using MatLAB® showed that the differences are only significant for the effect of tropical almond at confidence level of 90 % with p-value  $< 0.1$ . Details of the relationship between tropical almond concentration for the green synthesis and GO doping concentration versus bandgap energy of the green synthesized  $\text{TiO}_2$  are summarized in Fig. 14(a).

The bandgap energy of bare  $\text{TiO}_2$  and commercial  $\text{TiO}_2$  P25 measured in this work is 3.19 eV, close to the value of 3.22 eV obtained by Makula et al. [47] or 3.25 eV obtained by Tan et al. [49]. For  $\text{TiO}_2$  obtained from the green synthesis, the bandgap energy values are still in the range found by others. For example, Maurya et al. [27] obtained the bandgap value of 2.9 eV from *Bixa orallana* extract mediated green synthesized  $\text{TiO}_2$ , while Singh et al. [26] obtained the values 3.10, 3.31, 3.36 and 3.19 eV from different capping agent *Citrus limon* juice extract concentrations 0 %, 0.9 %, 0.45 %, and 0.27 % respectively. In another work, Nagaraj et al. [48] obtained the bandgap energy of 3.20, 3.15, and 3.09 eV from different  $\text{TiO}_2$  synthesis calcination temperatures of 550, 650, and 750 °C, respectively, whereas Purkait et al. [50] obtained the bandgap energy of 3.62 eV using direct bandgap calculation from *Trema orientalis* leaf extract mediated green synthesized  $\text{TiO}_2$ .

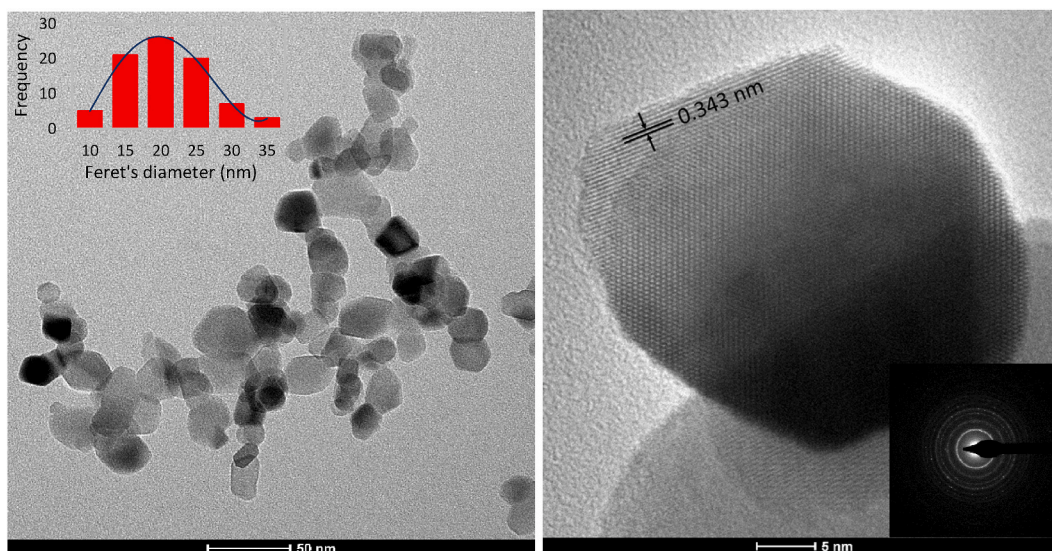


Fig. 7. TEM image and particle size distribution (left) and HRTEM image with lattice fringe and SAED pattern (right) of commercial TiO<sub>2</sub> P25.

### 3.3. Composition and surface morphology

Composition of the selected specimens and surface morphology of TiO<sub>2</sub> obtained from the green synthesis prepared at different tropical almond concentration and GO doping plus the one from commercial TiO<sub>2</sub> P25 were investigated using a field emission scanning electron microscope (FESEM) equipped with energy dispersive X-ray spectroscopy (EDX). The results of the elemental composition analysis from the energy dispersive X-ray spectroscopy for the selected specimen 1A, 2B, and 3B are given in Fig. 5. The elemental composition of Ti and O from sample 1A, and Ti, O, and C from sample 2B and 3B, all shown in Fig. 5 confirms the successfully green synthesis of TiO<sub>2</sub> using tropical almond extract as a capping agent and GO as a dopant. Since TiO<sub>2</sub> has poor conductivity, before FESEM observation, TiO<sub>2</sub> was coated using Au/Pd. These elements are detected as unlabeled peaks around 2 keV in the EDX spectra. The electron images of TiO<sub>2</sub> for specimen 1A-3C and commercial TiO<sub>2</sub> P25 are given in Fig. 6 with a scale bar of 5 μm.

The field emission scanning electron microscope was used to elucidate the influences of tropical almond extract medium and GO addition during the green synthesis on the surface morphology of TiO<sub>2</sub>. As can be seen in Fig. 6, the electron images reveal the surface morphology of TiO<sub>2</sub> particles. For the synthesized TiO<sub>2</sub>, particles with round shapes are clearly found showing good distribution within the specimens for most of the synthesized TiO<sub>2</sub> except for the pristine TiO<sub>2</sub> (1A). For this pristine TiO<sub>2</sub> synthesized regularly using ethanol with no tropical almond extract nor GO doping addition, the particles tend to form chunks and clump together with irregular particle size and shape. With the addition of tropical almond extract as a capping agent (1B and 1C), round shape particles appear replacing the chunks and the particle size of TiO<sub>2</sub> tends to get homogeneous with the increase of tropical almond concentration, agrees with the results obtained by Rajendhiran et al. [28].

For TiO<sub>2</sub> synthesized using ethanol with small amount of GO doping concentration but no tropical almond (2A), the particles seem to have perfect round shape but with more variations in size. Using the same GO concentration but with the addition of tropical almond, the particle size tends to get smaller (2B and 2C) with homogeneous distribution. The addition of more GO doping concentration (3A) maintains the particle shape, and again, with the addition of more tropical almond concentration reduces the TiO<sub>2</sub> particle size (3B and 3C). From this finding, it is obvious that tropical almond extract affects the formation of TiO<sub>2</sub> particles during the green synthesis. The same is true for the addition of GO doping; however, with more GO concentration, the round particle gets bigger, consistent with the TEM results given in Fig. 8. For the commercial TiO<sub>2</sub> P25, the FESEM image presents sphere-like particles in an agglomerated manner with a homogeneous average particle size of 30 nm, agrees with our previous results [51].

For clarity in the particle size, high resolution transmission electron microscopy (HRTEM) images along with selected area diffraction (SAED) were taken using transmission electron microscope and the results are given in Fig. 7 for the commercial TiO<sub>2</sub> P25 and Fig. 8 for the selected specimens 1A, 2B, and 3B. Using the ImageJ software [52], the spacing between the crystal planes for specimen 1A, 2B, 3B, and P25 was obtained to be 0.350 nm, 0.353 nm, 0.357 nm, and 0.343 nm, respectively. The homogeneous shape and the small size of nanoparticles are very beneficial for photovoltaic activity: smaller grain size has a larger surface area, leading to better interaction with photon. In this work, as has been previously stated, tropical almond extract and GO doping affect the formation of TiO<sub>2</sub> particles during the green synthesis. With no tropical almond and GO, the formation of TiO<sub>2</sub> is merely controlled by hydrolysis and condensation reactions [53]. In the presence of tropical almond fruits extracts as a capping agent and or GO as a dopant, there will be other factors that control the growth during the green synthesis. The proposed formation mechanism for the green synthesis of TiO<sub>2</sub> nanoparticles in the presence of tropical almond fruits extracts and GO is schematically presented in Fig. 9.

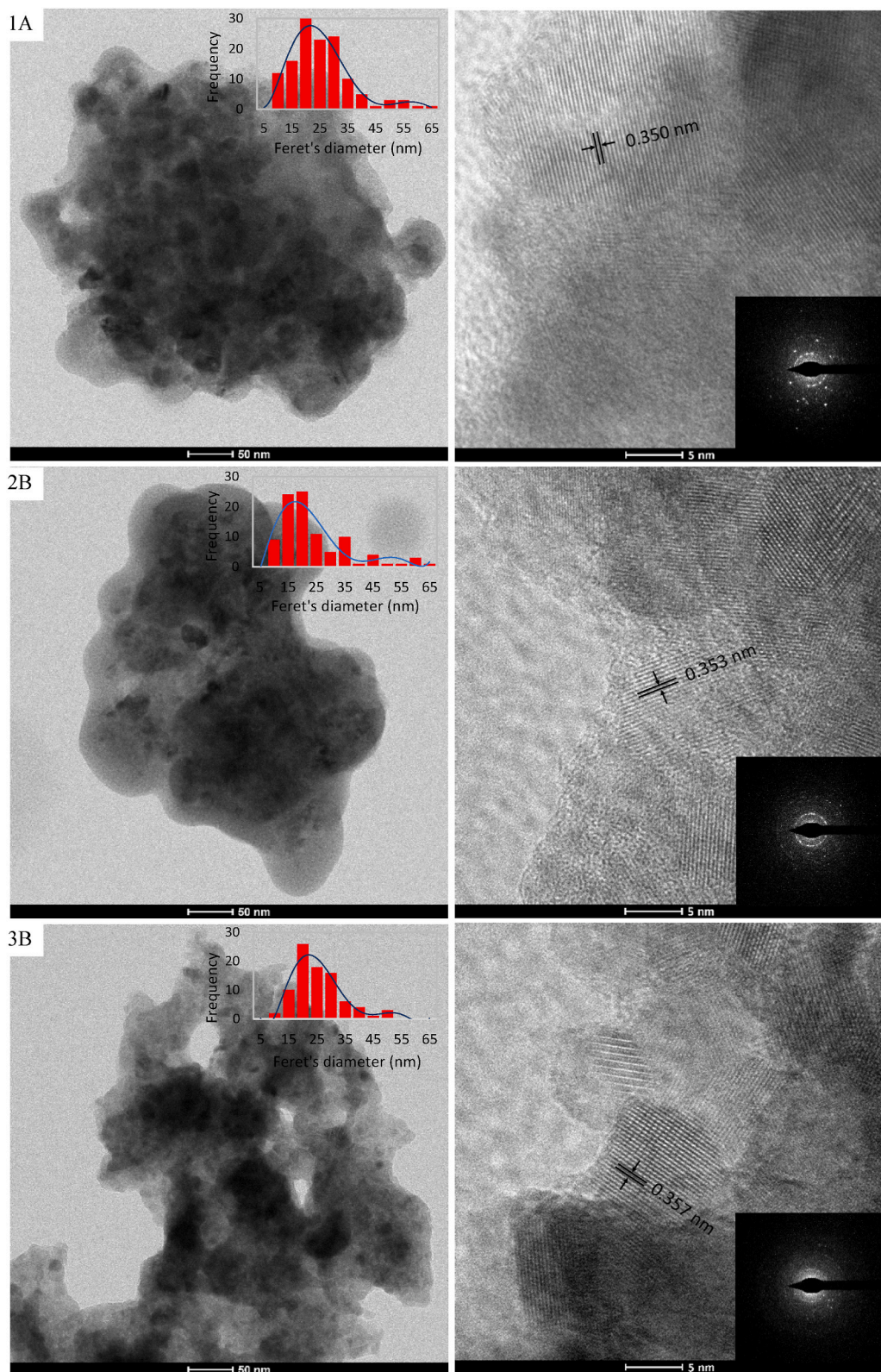


**Fig. 8.** TEM image with particle size distribution (left) and HRTEM with lattice fringe and SAED pattern (right) of TiO<sub>2</sub> from the green synthesis with variations represented by sample 1A, 2B, and 3B.

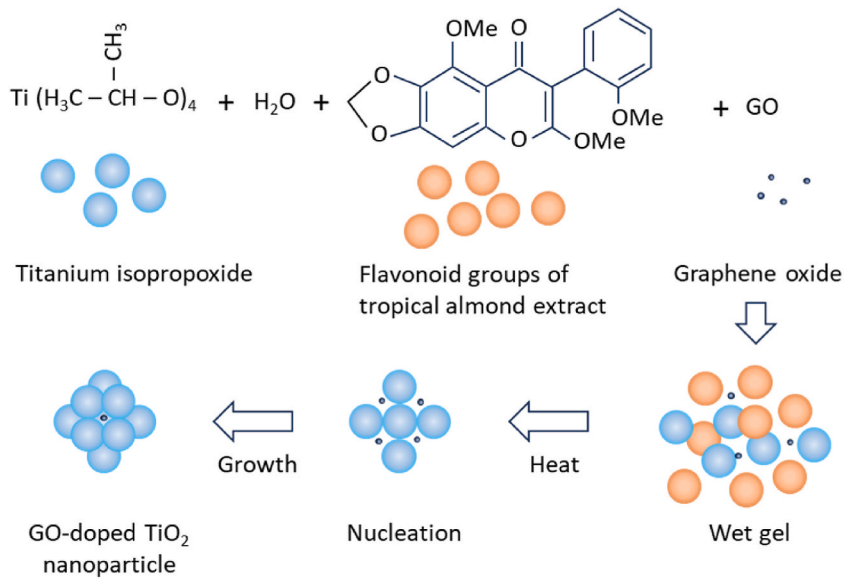


Fig. 9. Schematic diagram of the proposed formation mechanism for the green synthesis of  $TiO_2$  nanoparticles in the presence of tropical almond fruits extracts and GO.

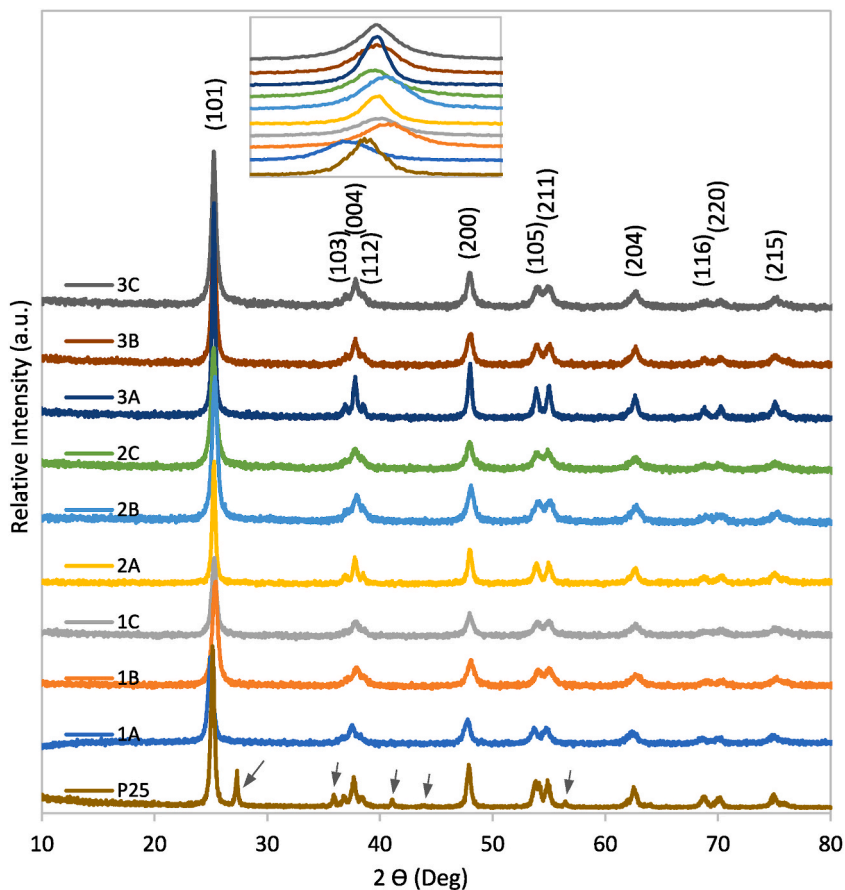
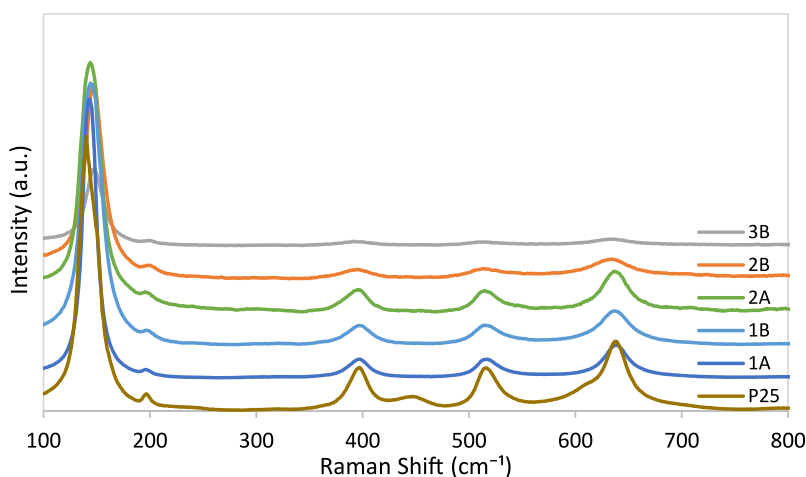


Fig. 10. Superimposed X-ray diffractograms of  $TiO_2$  obtained from the green synthesis with single phase of anatase and from the commercial  $TiO_2$  P25 with two phases of anatase and rutile (rutile is indicated by the arrow). The inset shows (101) peak shifting.

**Table 3**Lattice parameters and crystallite size of TiO<sub>2</sub> with sample variations. Standard errors are given in the parenthesis.

Sample	Lattice parameter			Goodness of fit ( $\chi^2$ )	Crystallite size (nm)
	a (Å)	c (Å)	V (Å) <sup>3</sup>		
1A	3.7843	9.4980	136.0166	1.20	12.53 (0.56)
1B	3.7901	9.5035	136.5164	1.00	10.43 (0.18)
1C	3.7884	9.5046	136.4055	1.06	12.93 (0.54)
2A	3.7869	9.5077	136.3426	1.05	16.30 (0.85)
2B	3.7883	9.5020	136.3672	1.00	11.83 (0.71)
2C	3.7880	9.5000	136.3150	1.02	9.31 (0.08)
3A	3.7860	9.5066	136.2613	1.00	18.32 (0.74)
3B	3.7876	9.5084	136.4067	1.03	13.61 (0.71)
3C	3.7902	9.5065	136.5631	1.00	11.62 (0.65)
P25	3.7870	9.5090	136.3721	1.20	17.03 (0.02)

**Fig. 11.** Superimposed Raman spectra of TiO<sub>2</sub> obtained from the green synthesis represented by samples 1A, 1B, 2A, 2B, 3B, and the one from commercial TiO<sub>2</sub> P25.

### 3.4. Crystallographic properties

Powder X-ray diffraction was used to analyze the crystallographic properties of TiO<sub>2</sub> obtained from the green synthesis prepared at different tropical almond and GO concentrations plus the one from commercial TiO<sub>2</sub> P25 as a comparison and the results are given in Fig. 10. All diffractograms from the green synthesis reveal prominent peaks at around 25.3°, 38.4°, 48.1°, 55.0°, 62.6°, 68.7°, 74° corresponding to the (101), (004), (200), (211), (204), (116) and (215) planes, respectively. The results from samples 1B and 1C confirmed the results obtained by Rajendhiran et al. [28]. These peaks belong to tetragonal anatase phase with space group  $I4_1/amd$  (ICSD 98-015-4604). A very low intensity peak detected at around 31.6° is possibly due to the presence of TiO<sub>2</sub> with brookite phase [54]. The diffractogram of commercial TiO<sub>2</sub> P25 shows the same peaks as the green synthesized TiO<sub>2</sub> corresponding to tetragonal anatase phase and other prominent peaks at 27.32°, 35.84°, 41.12°, and 41.12° corresponding to the (110), (101), (111), and (120) planes, respectively, of tetragonal rutile phase with space group  $I4_2/mnm$  (ICSD 98-003-3839). These findings are in line with the results obtained by others [7,9,55] and confirm our previous works [51,54,56]. The lattice constants and the goodness of fit ( $\chi^2$ ) after Rietveld analysis for all samples are given in Table 3.

Sharp and strong peaks indicated by each variation reveal a high crystalline nature of the prepared samples and there are no other new peaks detected with the addition of tropical almond extracts or GO doping. It can be assumed that tropical almond extract and GO dopant addition have not disrupted the crystallographic formation of TiO<sub>2</sub> during the green synthesis. Slight shifting of the peaks, however, are observed in all the green synthesized TiO<sub>2</sub> to the higher angle as compared to that of TiO<sub>2</sub> P25 as can be inspected in the plane (101) inset Fig. 10, possibly due to crystallite size and lattice strain that affect the Bragg peak by increasing the peak width and intensity and shifting the peak angle accordingly [57].

The average crystallite size of each sample was calculated from all diffraction peaks using the Scherrer formula [50,57,58]. In this calculation, considering the wavelength of X-ray radiation of Cu K $\alpha$  (0.15406 nm) at full width at half maximum (FWHM) and a constant of 0.89, the average crystallite size of commercial TiO<sub>2</sub> P25 of 17.03 nm was obtained. Using the same calculation, the average crystallite size of sample 1A, 1B, and 1C was 12.53 nm, 10.43 nm, and 12.93 nm, respectively. Different from the results obtained by Rejendhiran et al. [28], for sample 1B and 1C, the crystallite size of 1B (0.6 %) was smaller than that of 1C (0.8 %). This

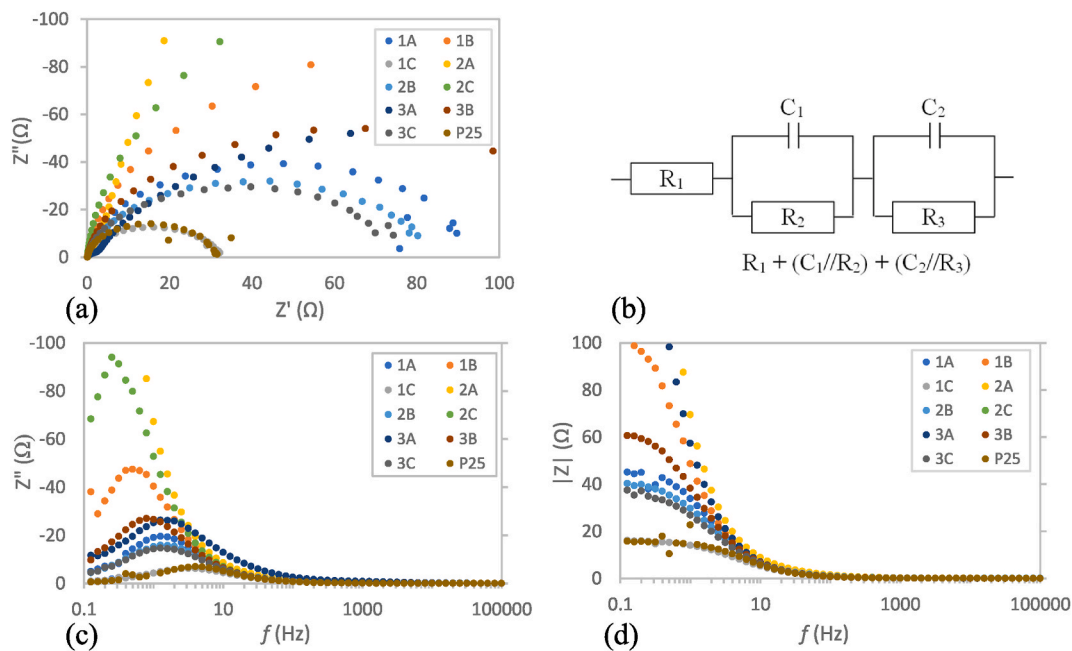


**Fig. 12.** Impedance spectra of the DSSC device measured under room light condition: (a) Nyquist representation, (b) the equivalent circuit model, (c) Bode imaginary, and (d) Bode magnitude.

difference could be due to the facts that different geographical areas, different altitudes, and climates could have the same chemical content but in different ratios or even different chemical contents [59,60] that might affect the crystal formation. The average crystallite size of sample 2A, 2B, and 2C was 16.30 nm, 11.83 nm, and 9.31 nm, respectively, whereas the average crystallite size of sample 3A, 3B, and 3C was 18.32 nm, 13.61 nm, and 11.62 nm, respectively. These results are tabulated in Table 3 along with the standard error in the bracket. The crystallite sizes obtained in this work are consistent with the particle sizes observed in the TEM images given in Figs. 7 and 8 for the green synthesis and the one from the commercial TiO<sub>2</sub> P25, respectively.

In general, two-way ANOVA showed that there is a significant difference among the variables at confidence level of 90 % with p-value of 0.005 and 0.09 for tropical almond addition and GO doping, respectively. One-way ANOVA showed that there is a slight difference in the crystallite size of sample 1A, 1B, and 1C; however, the value is independent of the treatment and the difference is insignificant. For the samples with GO doping and the addition of tropical almond extract (2A – 3C), there is consistencies in which the crystallite size decreases with the increase of tropical almond extract addition, and thus it is assumed that this decrease in crystallite size is accredited to the extract solution that prevents coalescence of the crystallites and inhibits the particle growth during the green synthesis. This consistency is significant with p-value 0.08 and 0.1 for GO doping concentration 0.0017 % (2A – 2C) and 0.16 % (3A – 3C), respectively. On the contrary, with the addition of GO alone, there is a tendency of increase in the crystallite size (1A, 2A, 3A). The same is true for low concentration of tropical almond and GO (1B, 2B, 3B); however, at higher concentration of tropical almond and GO (1C, 2C, 3C), the crystallite size is independent of treatment. The difference, however, is statistically insignificant (p-value = 0.2). Details of the relationship between tropical almond concentration for the green synthesis and GO doping concentration versus crystallite size of the green synthesized TiO<sub>2</sub> are summarized in Fig. 14(b).

### 3.5. Raman spectroscopy

Information on the chemical structure, phase, crystallinity, and molecular interactions of TiO<sub>2</sub> was further examined using Raman spectroscopy. The Raman spectra of TiO<sub>2</sub> obtained from the green synthesis represented by sample 1A, 2B, and 3B and the one from the commercial TiO<sub>2</sub> P25 are given in Fig. 11 for the region 800–100 cm<sup>-1</sup>.

The spectrum of commercial TiO<sub>2</sub> P25 shows a strong characteristic of anatase phase, together with the weak bands from rutile phase. These characteristics are indicated by the peaks centering at 143 cm<sup>-1</sup>, 199 cm<sup>-1</sup>, 398 cm<sup>-1</sup>, 516 cm<sup>-1</sup> and 638 cm<sup>-1</sup>, which are attributed to the anatase phase [61], while another weak peak, located at 448 cm<sup>-1</sup>, is characteristic of the rutile phase [62]. It then can be confirmed that the commercial TiO<sub>2</sub> P25 contains a mixture of anatase and low amount of rutile phases. The Raman spectra of TiO<sub>2</sub> obtained from the green synthesis are represented by sample 1A, 1B, 2A, 2B, and 3B only. The spectrum of sample 1A reveals that it has the same characteristics as commercial TiO<sub>2</sub> P25 except at 448 cm<sup>-1</sup> because 1A contains anatase only. Other TiO<sub>2</sub> spectra from 1B, 2A, 2B, and 3B are all present in the pure anatase phase with a slight blue shifted [63,64] as indicated by the corresponding five characteristics with the principal peak locating around 144–146 cm<sup>-1</sup> and other peaks at 199–200 cm<sup>-1</sup>, 398 cm<sup>-1</sup>, 516 cm<sup>-1</sup> and 638 cm<sup>-1</sup>. This finding is consistent with the XRD patterns given in Fig. 10.

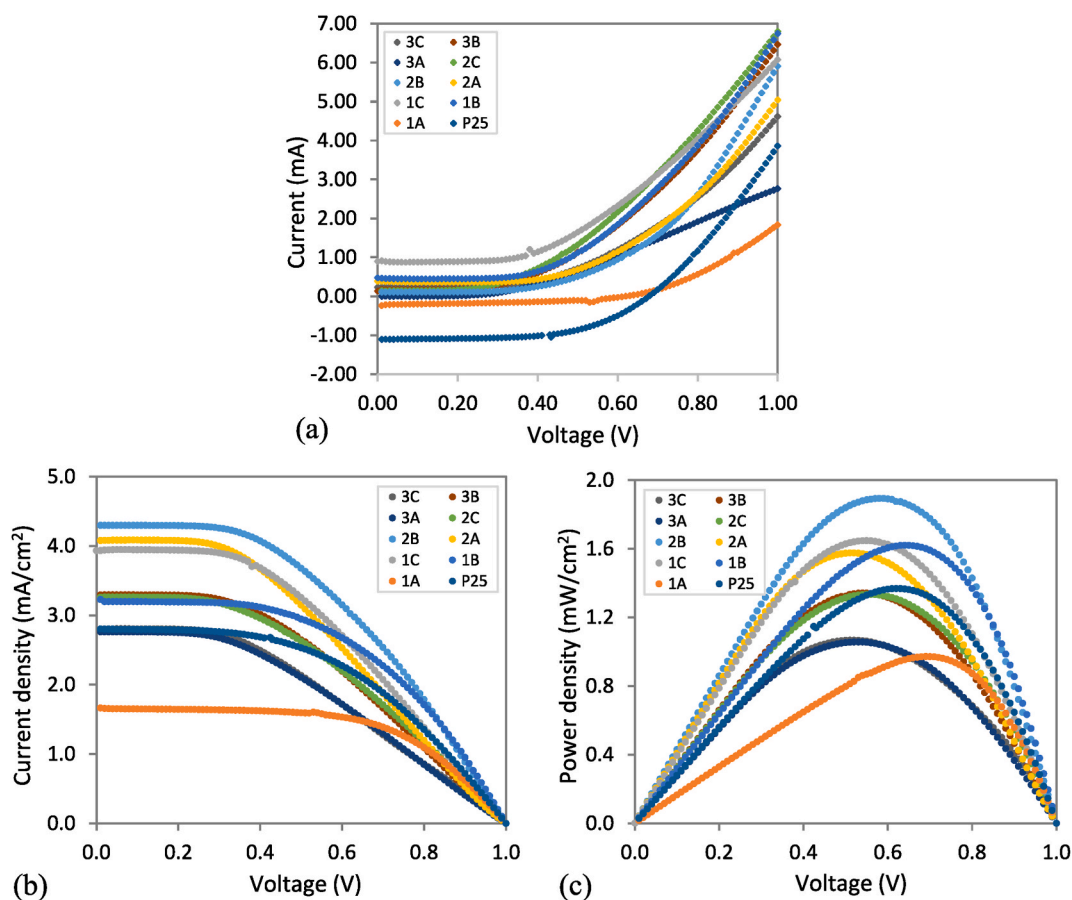


**Fig. 13.** I–V characteristic (a), current density (b) and power density (c) curves of the DSSC devices fabricated using  $\text{TiO}_2$  obtained from the green synthesis with sample variations 1A–3C and from the commercial  $\text{TiO}_2$  P25.

### 3.6. Electrochemical study

The electrochemical characteristics of the DSSC device were examined using EIS to reveal the internal kinetics and reactions of the DSSC and the results are given in Fig. 12. The electrochemical characteristics of the DSSC devices are represented in the forms of impedance spectra of Nyquist plots given in Fig. 12(a) with an equivalent circuit model given in Fig. 12(b), Bode imaginary corresponding to the Nyquist plots given in Fig. 12(c), and Bode magnitude diagrams given in Fig. 12(d).

As indicated by the Nyquist plot drawn on the real and imaginary impedance given in Fig. 12(a), the electrochemical characteristics of all DSSC devices show a similar semicircle representing the interface resistance of electrons but with a different value indicated by the differences in the semicircle radius. In an ascending order, the smallest semicircle radius is given by sample 1C followed by P25, 3C, 2B, 1A, 3B, 3A, 1B, 2C, 2A. These electrochemical characteristics, however, do not necessarily have a linear relationship with the power conversion efficiency as evidenced by the results obtained from photovoltaic activities given in the next section.

A semicircle radius indicates the charge transfer resistance [65]. The equivalent circuit model of the DSSC device is schematically given in Fig. 12(b) in which  $R_1$  is the serial resistance of FTO glass,  $C_1//R_2$  is the impedance at  $\text{TiO}_2/\text{dye}/\text{electrolyte}$  interface, and  $C_2//R_3$  is the impedance at the counter electrode/electrolyte interface. As for the Nyquist plots, the same trends can be observed in the Bode imaginary plots, imaginary parts of the impedance vs. frequency, as can be seen in Fig. 12(c). The Bode imaginary plots show that the peaks related to the recombination processes at the  $\text{TiO}_2/\text{electrolyte}$  interface [66] shifted toward higher frequencies. For the Bode magnitude diagrams given in Fig. 12(d), at high frequency regions, the Z values tend towards zero that indicate the decrease in the resistance of the materials [67].

### 3.7. Photovoltaic activity

To analyze the DSSC performance, the photovoltaic activity was analyzed. The resulting I–V characteristic, current density (J–V), and power density (P–V) curves are given in Fig. 13(a) Fig. 13(b) and 13(c), respectively, and were used to calculate power conversion efficiencies (PCE) [68], which are presented in Table 4. The device fabricated from commercial  $\text{TiO}_2$  P25 has a PCE of 1.44%. For the device fabricated from  $\text{TiO}_2$  obtained from the green synthesis, in samples with no GO additions, the performance increases with the

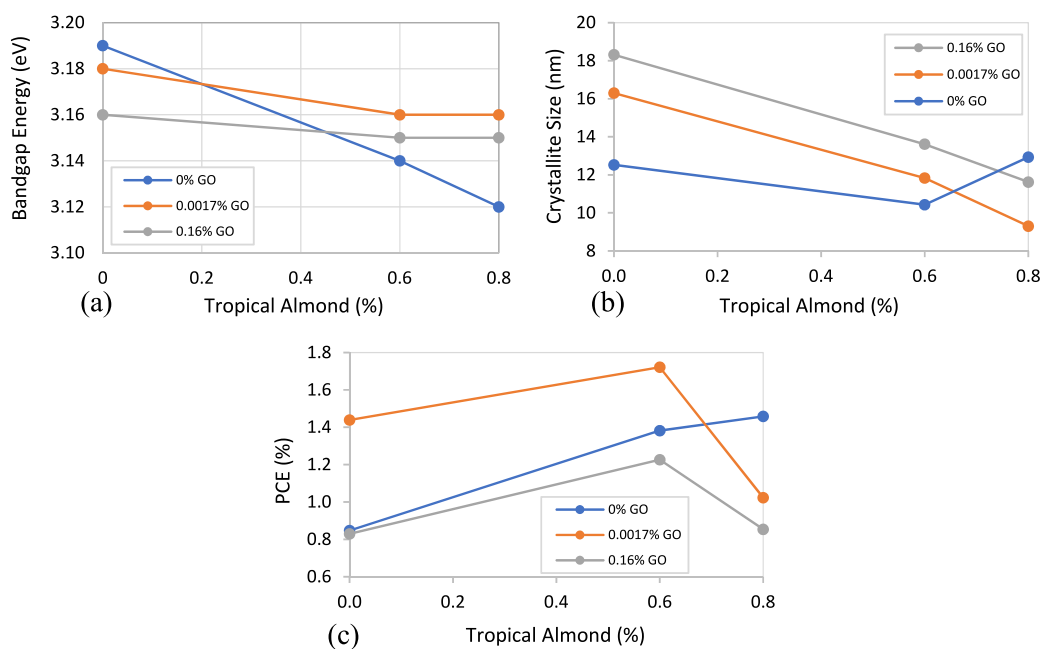


**Fig. 14.** Relationship between tropical almond concentration for the green synthesis and GO doping concentration vs. (a) bandgap energy, (b) crystallite size, and (c) the obtained DSSC device efficiency.

**Table 4**

Performance characteristics of the DSSC device fabricated using TiO<sub>2</sub> from the green synthesis and commercial P25. Standard errors are given in the parenthesis.

Sample	V <sub>oc</sub> (V)	J <sub>sc</sub> (mA/cm <sup>2</sup> )	FF	PCE (%)
1A	1.00	1.47	0.58	0.85 (0.02)
1B	1.00	2.70	0.53	1.38 (0.17)
1C	1.00	3.65	0.40	1.46 (0.06)
2A	0.96	3.91	0.39	1.44 (0.06)
2B	1.00	4.00	0.43	1.72 (0.09)
2C	0.99	2.62	0.38	1.02 (0.24)
3A	1.00	2.30	0.36	0.83 (0.04)
3B	0.95	3.20	0.39	1.22 (0.21)
3C	0.98	2.50	0.34	0.85 (0.15)
P25	1.00	3.80	0.39	1.44 (0.16)

addition of tropical almond concentration, namely 0.85 %, 1.38 %, and 1.46 % for sample 1A, 1B, and 1C, respectively. In the samples with 0.0017 % GO, the performance also increases from 2A to 2B, namely from 1.44 % to 1.72 %, but experiences a significant decrease to 1.02 % in sample 2C. The same trend also occurs in the samples with 0.16 % GO in which the performance increases from 0.83 % to 1.22 % and then decreases to 0.85 % for samples 3A, 3B, and 3C, respectively. In terms of GO alone, small GO concentration increases the performance from 0.85 % to 1.44 % for sample 1A and 2A, respectively, but decreases to 0.83 % with the increase of GO concentration for sample 3A. These results agree with the work of Shahid et al. [20]. The same trend also occurs with the same GO concentration in the medium containing small tropical almond concentration in which the performance increases from 1.38 % to 1.72 % for sample 1B and 2B, respectively, but decreases to 1.22 % for sample 3B. At higher tropical almond concentration, however, the trend is quite different in which the performance decreases with addition of GO concentrations. Details of the relationship between tropical almond concentration for the green synthesis and GO doping concentration versus the obtained DSSC device efficiency are summarized in Fig. 14(c).

As has been previously mentioned, excess concentration of GO doping does not result in a linear increase in efficiency. This shows that the addition of excess GO will reduce efficiency due to disrupting the role of the dye in light harvesting and in ideal electron recombination [18–20]. The same trends also occurred on the addition of tropical almond extract during the green synthesis, in which the highest performance with a power conversion efficiency of 1.72 % was obtained at an optimum condition only, i.e., from the device fabricated from TiO<sub>2</sub> green synthesized using tropical almond extract at concentration of 0.60 % and GO addition of 0.0017 %. In this instance, it seems that there must be an ideal ratio between the medium and GO doping concentration to optimally improve the DSSC performance. Nonetheless, the differences are statistically insignificant (*p*-value > 0.05). In the presence of GO, the schematics of DSSC

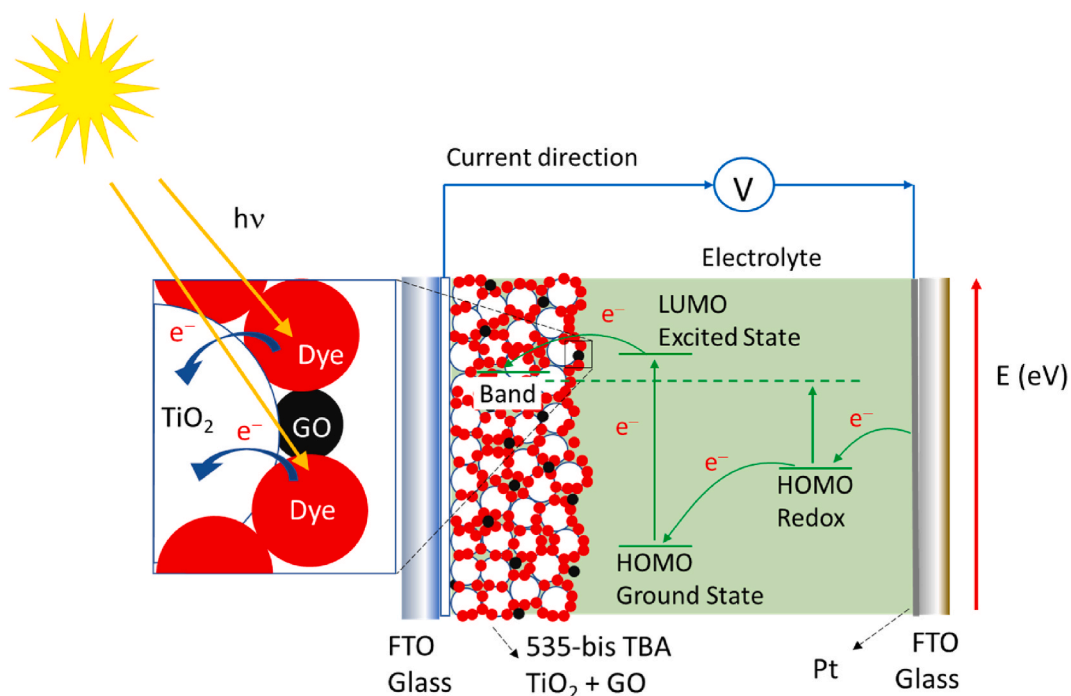


**Fig. 15.** Schematics of DSSC structure in the presence of GO and its electron transfer mechanisms along with electron paths through the energy of HOMO and LUMO levels and the current direction.

structure and electron transfer mechanisms along with electron paths through the energy of highest occupied molecular orbital (HOMO) and lowest unoccupied molecular orbital (LUMO) levels and the current direction in this work is schematically proposed in Fig. 15.

The efficiency obtained in this work is still low compared to the existing commercial silicon-based solar cells [2], however, the current PCE values are close to the PCE values obtained by other investigators. For example, in their work on performance enhancement of DSSCs using a natural sensitizer, Arifin et al. used N719 as a comparison with a PCE value of 1.29 % [40] whereas Sharma et al. obtained a PCE value of 4.81 % [69]. On the use of graphene based DSSCs, investigators such as Patil et al. obtained a PCE value of 4.43 % [70], Jeganathan et al. obtained a PCE value of 1.32 % [71], whereas Sadikin obtained a PCE value of 1.47 % [72]. Pavithra et al. [73] obtained PCE values of 0.0182 %, 0.0019 %, and 0.0039 % for pristine, flower, and seed of *Calotropis gigantea* extracts mediated green synthesized TiO<sub>2</sub>, respectively.

#### 4. Conclusion

The addition of tropical almond extract from a renewable natural resource could be used as a capping agent to control the growth of TiO<sub>2</sub> during the green synthesis, confirmed the work of Rajendhiran et al. Increasing the concentration of tropical almond extract could reduce the particle size and makes the distribution of particles more uniform. At certain concentration, tropical almond extract also succeeded in increasing the photocatalytic activity of TiO<sub>2</sub> by controlling the grain and crystallite sizes. At small tropical almond medium concentration, the addition of graphene oxide also increases the photocatalytic properties of TiO<sub>2</sub> and thus increases the performance of the DSSC device. Higher tropical almond medium concentration and addition of excess graphene oxide, however, reduce the performance of energy conversion efficiency due to disrupting the role of the dye in light harvesting and in ideal electron recombination. In this work, the composition of graphene oxide and tropical almond extract with the best performance succeeded in increasing the performance in the forms of energy conversion efficiency from 0.85 % to 1.72 %. As a comparison, power conversion efficiency from the commercial TiO<sub>2</sub> P25 has an energy conversion efficiency of 1.44 %. This finding is promising in terms of future works on the green synthesis of TiO<sub>2</sub> for potential application in the development DSSCs.

#### Funding

This work was supported by Universitas Indonesia under Hibah Publikasi Terindeks Internasional (PUTI) Q1 TA 2023–2024 No: NKB-537/UN2.RST/HKP.05.00/2023.

## Data availability

Data are available publicly at <https://data.mendeley.com/under the name 'GO doped Green Synthesized TiO<sub>2</sub> for DSSC.'> <https://doi.org/10.17632/ynjhzbfy8g.1>.

## CRedit authorship contribution statement

**Nofrijon Sofyan:** Writing – review & editing, Writing – original draft, Validation, Methodology, Funding acquisition, Formal analysis, Conceptualization. **Alry Mochtar Jamil:** Writing – original draft, Investigation, Data curation. **Aga Ridhova:** Visualization, Investigation, Data curation. **Akhmad Herman Yuwono:** Writing – review & editing. **Donanta Dhaneswara:** Writing – review & editing. **Jeffrey W. Fergus:** Writing – review & editing, Validation, Formal analysis.

## Declaration of competing interest

The authors declare that they have no known competing financial interests or personal relationships that could have appeared to influence the work reported in this paper.

## Acknowledgements

The authors acknowledge support from Integrated Laboratory and Research Center, Universitas Indonesia, and from Advanced Characterization Laboratories, National Research and Innovation Agency. The authors are also grateful to Dr. Mega Atria for the herbarium identification.

## Appendix A. Supplementary data

Supplementary data to this article can be found online at <https://doi.org/10.1016/j.heliyon.2024.e29370>.

## References

- [1] M.S. Islami, T. Urmee, I.N.S. Kumara, Developing a framework to increase solar photovoltaic microgrid penetration in the tropical region: a case study in Indonesia, *Oct. Sustain. Energy Technol. Assessments* 47 (2021) 101311 <https://doi.org/10.1016/J.SETA.2021.101311>.
- [2] Z.Y. Yeo, Z.P. Ling, J.W. Ho, Q.X. Lim, Y.H. So, S. Wang, Status review and future perspectives on mitigating light-induced degradation on silicon-based solar cells, *May, Renew. Sustain. Energy Rev.* 159 (2022) 112223, <https://doi.org/10.1016/J.RSER.2022.112223>.
- [3] N. Saad, M. Ibrahim, K.H. Sadok, M. Haouari, Fluoroborophosphate glasses doped with Cr<sup>3+</sup>, Nd<sup>3+</sup> and Yb<sup>3+</sup> as efficient light converters for silicon based solar cells, *Sep. J. Non-Cryst. Solids* 591 (2022) 121707 <https://doi.org/10.1016/J.JNONCRYSol.2022.121707>.
- [4] T. Saga, Advances in crystalline silicon solar cell technology for industrial mass production, *Jul. NPG Asia Mater.* 2 (3) (2010) 96–102, <https://doi.org/10.1038/asiamat.2010.82>.
- [5] M.A. Farhana, A. Manjeevan, J. Bandara, Recent advances and new research trends in Sb<sub>2</sub>S<sub>3</sub> thin film based solar cells, *Mar, J. Sci.: Advanced Materials and Devices* 8 (1) (2023) 100533, <https://doi.org/10.1016/j.jsamd.2023.100533>.
- [6] B. Ranamagar, I. Abiye, F. Abebe, Dye-sensitized solar cells on TiO<sub>2</sub> photoelectrodes sensitized with rhodamine, *Apr, Mater. Lett.* 336 (2023) 133887, <https://doi.org/10.1016/J.MATLET.2023.133887>.
- [7] S. Bhattarai, et al., A detailed review of perovskite solar cells: Introduction, working principle, modelling, fabrication techniques, future challenges, Elsevier Ltd, *Dec. 01., Micro and Nanostructures* 172 (2022), <https://doi.org/10.1016/j.micrna.2022.207450>.
- [8] J. Baxter, Commercialization of dye sensitized solar cells: present status and future research needs to improve efficiency, stability, and manufacturing, *Feb. J. Vac. Sci. Technol. A: Vacuum, Surfaces, and Films* 30 (2012) 20801 <https://doi.org/10.1116/1.3676433>.
- [9] R. Baby, P.D. Nixon, N.M. Kumar, M.S.P. Subathra, N. Ananthi, A comprehensive review of dye-sensitized solar cell optimal fabrication conditions, natural dye selection, and application-based future perspectives, 1, in: *Environmental Science and Pollution Research*, vol. 29, Springer Science and Business Media Deutschland GmbH, 2022, pp. 371–404, <https://doi.org/10.1007/s11356-021-16976-8>. Jan. 01.
- [10] A. Hagfeldt, G. Boschloo, L. Sun, L. Klöö, H. Pettersson, Dye-sensitized solar cells, *Nov. Chem Rev* 110 (11) (2010) 6595–6663, <https://doi.org/10.1021/cr900356p>.
- [11] I.C. Maurya, S. Senapati, S. Singh, P. Srivastava, P. Maiti, L. Bahadur, Effect of particle size on the performance of TiO<sub>2</sub> based dye-sensitized solar cells, *Sep. ChemistrySelect* 3 (34) (2018) 9872–9880, <https://doi.org/10.1002/slct.201801745>.
- [12] V.A. González-Verjan, et al., Effect of TiO<sub>2</sub> particle and pore size on DSSC efficiency, *Jul. Mater Renew Sustain Energy* 9 (2) (2020) <https://doi.org/10.1007/s40243-020-00173-7>.
- [13] M. Ashfaq, N. Talreja, N. Singh, D. Chauhan, 2D-Nanolayer (2D-nl)-based hybrid materials: a next-generation material for dye-sensitized solar cells, *MDPI*, Feb. 01, *Electronics (Switzerland)* 12 (3) (2023), <https://doi.org/10.3390/electronics12030570>.
- [14] A. Singh, et al., Property modulation of graphene oxide incorporated with TiO<sub>2</sub> for dye-sensitized solar cells, *Dec. ACS Omega* (2022) <https://doi.org/10.1021/acsomega.2c05637>.
- [15] E.M. Samsudin, S.B. Abd Hamid, Effect of band gap engineering in anionic-doped TiO<sub>2</sub> photocatalyst, *Appl. Surf. Sci.* 391 (Jan. 2017) 326–336, <https://doi.org/10.1016/j.apsusc.2016.07.007>.
- [16] L.G. Devi, B.N. Murthy, S.G. Kumar, Photocatalytic activity of TiO<sub>2</sub> doped with Zn<sup>2+</sup> and V<sup>5+</sup> transition metal ions: influence of crystallite size and dopant electronic configuration on photocatalytic activity, *Jan. Mater Sci Eng B Solid State Mater Adv Technol* 166 (1) (2010) 1–6, <https://doi.org/10.1016/j.mseb.2009.09.008>.
- [17] Y. Sun, et al., Surface chemistry and structure manipulation of graphene-related materials to address the challenges of electrochemical energy storage, *Jan. Chem. Commun.* 59 (18) (2023) 2571–2583, <https://doi.org/10.1039/d2cc06772b>.
- [18] H. Wang, S.L. Leonard, Y.H. Hu, Promoting effect of graphene on dye-sensitized solar cells, *Aug, Ind. Eng. Chem. Res.* 51 (32) (2012) 10613–10620, <https://doi.org/10.1021/ie300563h>.

- [19] Y. Zhang, H. Li, L. Kuo, P. Dong, F. Yan, Recent applications of graphene in dye-sensitized solar cells, 5–6, in: *Current Opinion in Colloid and Interface Science*, vol. 20, Elsevier Ltd, 2015, pp. 406–415, <https://doi.org/10.1016/j.cocis.2015.11.002>. Oct. 01.
- [20] M.U. Shahid, et al., Graphene loaded TiO<sub>2</sub> submicron spheres scattering layer for efficient dye-sensitized solar cell, *Chemosphere* 321 (2023) 138009, <https://doi.org/10.1016/j.chemosphere.2023.138009>.
- [21] K. Byrappa, T. Adschiri, Hydrothermal technology for nanotechnology, *Jun. Prog. Cryst. Growth Char. Mater.* 53 (2) (2007) 117–166, <https://doi.org/10.1016/j.pcrysgrow.2007.04.001>.
- [22] M. Aravind, M. Amalanathan, M.S.M. Mary, Synthesis of TiO<sub>2</sub> nanoparticles by chemical and green synthesis methods and their multifaceted properties, *Apr. SN Appl. Sci.* 3 (4) (2021) <https://doi.org/10.1007/s42452-021-04281-5>.
- [23] N. Seman, et al., Preparation method of titanium dioxide nanoparticles and its application: an update, in: *IOP Conference Series: Earth and Environmental Science*, Institute of Physics, 2022, <https://doi.org/10.1088/1755-1315/1091/1/012064>.
- [24] S. Vijayaram, et al., Applications of Green Synthesized Metal Nanoparticles — a Review, *Biological Trace Element Research*, Springer, 2023, <https://doi.org/10.1007/s12011-023-03645-9>.
- [25] N. Motakef-Kazemia, M. Yaqoubi, Green synthesis and characterization of bismuth oxide nanoparticle using mentha pulegium extract, *Iran. J. Pharm. Res. (IJPR)* 19 (2) (2020) 70–79, <https://doi.org/10.22037/ijpr.2019.15578.13190>.
- [26] S. Singh, I.C. Maurya, A. Tiwari, P. Srivastava, L. Bahadur, Green synthesis of TiO<sub>2</sub> nanoparticles using Citrus limon juice extract as a bio-capping agent for enhanced performance of dye-sensitized solar cells, *Surface. Interfac.* 28 (Feb) (2022), <https://doi.org/10.1016/j.surfin.2021.101652>.
- [27] I.C. Maurya, S. Singh, S. Senapati, P. Srivastava, L. Bahadur, Green synthesis of TiO<sub>2</sub> nanoparticles using Bixa orellana seed extract and its application for solar cells, *Dec. Sol. Energy* 194 (2019) 952–958, <https://doi.org/10.1016/j.solener.2019.10.090>.
- [28] R. Rajendhiran, V. Deivasigamani, J. Palanisamy, S. Masan, S. Pitchaiya, Terminalia catappa and carissa carandas assisted synthesis of TiO<sub>2</sub> nanoparticles - a green synthesis approach, in: *Materials Today: Proceedings*, Elsevier Ltd, 2021, pp. 2232–2238, <https://doi.org/10.1016/j.matpr.2020.10.223>.
- [29] L. Thomson, B. Evans, *Terminalia catappa*, vol. 2019, *The IUCN Red List of Threatened Species*, 2019 e.T61989853A61989855.
- [30] O.V. Kharisova, H.V.R. Dias, B.I. Kharisov, B.O. Pérez, V.M.J. Pérez, The greener synthesis of nanoparticles, *Apr. Trends Biotechnol.* 31 (4) (2013) 240–248, <https://doi.org/10.1016/j.tibtech.2013.01.003>.
- [31] P. Singh Jassal, D. Kaur, R. Prasad, J. Singh, Green synthesis of titanium dioxide nanoparticles: development and applications, *J Agric Food Res* 10 (Dec) (2022), <https://doi.org/10.1016/j.jafr.2022.100361>.
- [32] J.H. Yum, E. Baranoff, S. Wenger, M.K. Nazeeruddin, M. Grätzel, Panchromatic engineering for dye-sensitized solar cells, *Mar. Energy Environ. Sci.* 4 (3) (2011) 842–857, <https://doi.org/10.1039/c0ee00536c>.
- [33] S. Ng, O. Lasekan, K. Muhammad, R. Sulaiman, N. Hussain, Effect of roasting conditions on color development and Fourier transform infrared spectroscopy (FTIR-ATR) analysis of Malaysian-grown tropical almond nuts (*Terminalia catappa* L.), *Cardiovasc Interv Ther* 8 (1) (Sep. 2014), <https://doi.org/10.1186/s13065-014-0055-2>.
- [34] M. Sampath, M. Vasanthi, Isolation, structural elucidation of flavonoids from polyalthia longifolia (sonn.) thawaites and evaluation of antibacterial, antioxidant and anticancer potential, *Int. J. Pharm. Pharmaceut. Sci.* 5 (1) (2013) 336–341.
- [35] M.C. Dias, D.C.G.A. Pinto, A.M.S. Silva, Plant flavonoids: chemical characteristics and biological activity, *MDPI*, Sep. 01, *Molecules* 26 (17) (2021), <https://doi.org/10.3390/molecules26175377>.
- [36] A. Zdyb, S. Krawczyk, Natural flavonoids as potential photosensitizers for dye-sensitized solar cells, *Mar. Ecological Chemistry and Engineering S* 26 (1) (2019) 29–36, <https://doi.org/10.1515/eces-2019-0016>.
- [37] V.H. Pham, et al., Chemical functionalization of graphene sheets by solvothermal reduction of a graphene oxide suspension in N-methyl-2-pyrrolidone, *Mar. J. Mater. Chem.* 21 (10) (2011) 3371–3377, <https://doi.org/10.1039/c0jm02790a>.
- [38] D. Khalili, Graphene oxide: a promising carbocatalyst for the regioselective thiocyanation of aromatic amines, phenols, anisols and enolizable ketones by hydrogen peroxide/KSCN in water, *New J. Chem.* 40 (3) (2016) 2547–2553, <https://doi.org/10.1039/c5nj02314a>.
- [39] Z. Ciplak, N. Yildiz, A. Çalimli, Investigation of graphene/Ag nanocomposites synthesis parameters for two different synthesis methods, *Apr. Fullerenes, Nanotub. Carbon Nanostruct.* 23 (4) (2015) 361–370, <https://doi.org/10.1080/1536383X.2014.894025>.
- [40] Z. Arifin, S. Soeparman, D. Widhiyanuriyawan, S. Suyitno, Performance enhancement of dye-sensitized solar cells using a natural sensitizer, *Int. J. Photoenergy* 2017 (2017), <https://doi.org/10.1155/2017/2704864>.
- [41] C.Y. Cai, S.K. Tseng, M. Kuo, K.Y. Andrew Lin, H. Yang, R.H. Lee, Photovoltaic performance of a N719 dye based dye-sensitized solar cell with transparent macroporous anti-ultraviolet photonic crystal coatings, *RSC Adv.* 5 (124) (2015) 102803–102810, <https://doi.org/10.1039/c5ra21194h>.
- [42] F. Hirose, M. Shikaku, Y. Kimura, M. Niwano, IR study on N719 dye adsorption with high temperature dye solution for highly efficient dye-sensitized solar cells, *J. Electrochem. Soc.* 157 (11) (2010) B1578, <https://doi.org/10.1149/1.3485036>.
- [43] N.C.T. Martins, J. Angelo, A.V. Girão, T. Trindade, L. Andrade, A. Mendes, N-doped carbon quantum dots/TiO<sub>2</sub> composite with improved photocatalytic activity, *Sep. Appl. Catal., B* 193 (2016) 67–74, <https://doi.org/10.1016/j.apcatb.2016.04.016>.
- [44] P. Praveen, G. Viruthagiri, S. Mugundan, N. Shanmugam, Structural, optical and morphological analyses of pristine titanium di-oxide nanoparticles - synthesized via sol-gel route, *Spectrochim. Acta Mol. Biomol. Spectrosc.* 117 (2014) 622–629, <https://doi.org/10.1016/j.saa.2013.09.037>.
- [45] A. Khalilzadeh, S. Fatemi, Spouted bed reactor for VOC removal by modified nano-TiO<sub>2</sub> photocatalytic particles, *Nov. Chem. Eng. Res. Des.* 115 (2016) 241–250, <https://doi.org/10.1016/j.chemd.2016.10.004>.
- [46] B.H. Stuart, *Infrared Spectroscopy: Fundamentals and Applications*, Wiley, West Sussex, 2004, <https://doi.org/10.1002/0470011149>.
- [47] P. Makula, M. Pacia, W. Macyk, How to correctly determine the band gap energy of modified semiconductor photocatalysts based on UV-vis spectra, 23, in: *Journal of Physical Chemistry Letters*, vol. 9, American Chemical Society, 2018, pp. 6814–6817, <https://doi.org/10.1021/acs.jpclett.8b02892>. Dec. 06.
- [48] G. Nagaraj, A.D. Raj, A.A. Irudayaraj, R.L. Josephine, Tuning the optical band Gap of pure TiO<sub>2</sub> via photon induced method, *Optik* 179 (Feb. 2019) 889–894, <https://doi.org/10.1016/j.ijleo.2018.11.009>.
- [49] L.L. Tan, W.J. Ong, S.P. Chai, A.R. Mohamed, Band gap engineered, oxygen-rich TiO<sub>2</sub> for visible light induced photocatalytic reduction of CO<sub>2</sub>, *Jun. Chem. Commun.* 50 (52) (2014) 6923–6926, <https://doi.org/10.1039/c4cc01304b>.
- [50] P.K. Purkait, S. Majumder, S. Roy, S. Maitra, G. Chandra Das, M.G. Chaudhuri, Enhanced heterogeneous photocatalytic degradation of florasulam in aqueous media using green synthesized TiO<sub>2</sub> nanoparticle under UV light irradiation, *Sep. Inorg. Chem. Commun.* 155 (2023) 111017 <https://doi.org/10.1016/j.inoche.2023.111017>.
- [51] N. Sofyan, A. Ridhova, A.H. Yuwono, A. Udhiarto, Fabrication of solar cells with TiO<sub>2</sub> nanoparticles sensitized using natural dye extracted from mangosteen pericarps, *International Journal of Technology* 8 (7) (2017) 1229–1238, <https://doi.org/10.14716/ijtech.v8i7.692>.
- [52] C.A. Schneider, W.S. Rasband, K.W. Eliceiri, NIH Image to ImageJ: 25 years of image analysis, *Nat. Methods* 9 (7) (2012) 671–675, <https://doi.org/10.1038/nmeth.2089>.
- [53] S. Mustapha, et al., Application of TiO<sub>2</sub> and ZnO nanoparticles immobilized on clay in wastewater treatment: a review, 1, in: *Applied Water Science*, vol. 10, Springer Science and Business Media Deutschland GmbH, 2020, <https://doi.org/10.1007/s13201-019-1138-y>. Jan. 01.
- [54] N. Sofyan, A. Ridhova, A.H. Yuwono, A. Udhiarto, J.W. Fergus, Synthesis of TiO<sub>2</sub> nanoparticles at low hydrothermal temperature and its performance for DSSC sensitized using natural dye extracted from *Melastoma malabathricum* L. seeds, *Sep. Int. J. Energy Res.* 43 (11) (2019) 5959–5968, <https://doi.org/10.1002/er.4710>.
- [55] R.S. Dubey, K.V. Krishnamurthy, S. Singh, Experimental studies of TiO<sub>2</sub> nanoparticles synthesized by sol-gel and solvothermal routes for DSSCs application, *Results Phys.* 14 (Sep) (2019), <https://doi.org/10.1016/j.rinp.2019.102390>.
- [56] N. Sofyan, A. Ridhova, A.H. Yuwono, A. Udhiarto, Preparation of anatase TiO<sub>2</sub> nanoparticles using low hydrothermal temperature for dye-sensitized solar cell, in: *IOP Conference Series: Materials Science and Engineering*, 2018, <https://doi.org/10.1088/1757-899X/316/1/012055>.
- [57] A. Khorsand Zak, W. H. Abd Majid, M.E. Abrishami, R. Yousefi, X-ray analysis of ZnO nanoparticles by Williamson-Hall and size-strain plot methods, *Jan. Solid State Sci.* 13 (1) (2011) 251–256, <https://doi.org/10.1016/j.solidstatesciences.2010.11.024>.

- [58] B.D. Cullity, S.R. Stock, *Elements of X-Ray Diffraction*, third ed., Pearson, Essex, 2014.
- [59] A. Mannu, S. Melito, G.L. Petretto, P. Manconi, G.M. Pintore, M. Chessa, Geographical variation of the chemical composition in essential oils extracted from Sardinian *Salvia verbenaca*, *Nat. Prod. Res.* 36 (1) (2022) 367–370, <https://doi.org/10.1080/14786419.2020.1788021>.
- [60] S. Melito, G.L. Petretto, J. Podani, M. Foddai, M. Maldini, M. Chessa, G. Pintore, Altitude and climate influence *Helichrysum italicum* subsp. *microphyllum* essential oils composition, *Feb. Ind. Crop. Prod.* 80 (2016) 242–250, <https://doi.org/10.1016/j.indcrop.2015.11.014>.
- [61] W. Su, J. Zhang, Z. Feng, T. Chen, P. Ying, C. Li, Surface phases of TiO<sub>2</sub> nanoparticles studied by UV Raman spectroscopy and FT-IR spectroscopy, *May, J. Phys. Chem. C* 112 (20) (2008) 7710–7716, <https://doi.org/10.1021/jp7118422>.
- [62] H.C. Choi, Y.M. Jung, S. Bin Kim, Size effects in the Raman spectra of TiO<sub>2</sub> nanoparticles, *Jan. Vib. Spectrosc.* 37 (1) (2005) 33–38, <https://doi.org/10.1016/j.vibspec.2004.05.006>.
- [63] R. Taziwa, E. Meyer, N. Takata, Structural and Raman spectroscopic characterization of C-TiO<sub>2</sub> nanotubes synthesized by a template-assisted sol-gel technique, *J. Nanosci. Nanotechnol. Res* 1 (1:4) (2017) 1–11.
- [64] K.I. Hadjiivanov, et al., Power of infrared and Raman spectroscopies to characterize metal-organic frameworks and investigate their interaction with guest molecules, *American Chemical Society, Chem. Rev.* 121 (3) (2021) 1286–1424, <https://doi.org/10.1021/acs.chemrev.0c00487>. Feb. 10.
- [65] U. Mehmood, et al., Electrochemical impedance spectroscopy and photovoltaic analyses of dye-sensitized solar cells based on carbon/TiO<sub>2</sub> composite counter electrode, *J. Electrochem. Soc.* 163 (5) (2016) H339–H342, <https://doi.org/10.1149/2.0111606jes>.
- [66] S. Sarker, H.W. Seo, D.M. Kim, Electrochemical impedance spectroscopy of dye-sensitized solar cells with thermally degraded N719 loaded TiO<sub>2</sub>, *Chem. Phys. Lett.* 585 (2013) 193–197, <https://doi.org/10.1016/j.cplett.2013.08.101>.
- [67] L. Wei, et al., Effect of different donor groups in bis(6-methoxypyridin-2-yl) substituted co-sensitizer on the performance of N719 sensitized solar cells, *Nov. RSC Adv.* 5 (117) (2015) 96934–96944, <https://doi.org/10.1039/c5ra19417b>.
- [68] N. Kutlu, Investigation of electrical values of low-efficiency dye-sensitized solar cells (DSSCs), *May, Energy* 199 (2020), <https://doi.org/10.1016/j.energy.2020.117222>.
- [69] G. Sharma, C. Dawo, K. Mulchandani, U.K. Kumawat, R.K. Singhal, C. Lal, Revealing the photophysics of N719 dye based dye-sensitized solar cell, *Opt. Mater.* 142 (2023) 114113, <https://doi.org/10.1016/j.optmat.2023.114113>.
- [70] J.V. Patil, S.S. Mali, J.S. Shaikh, A.P. Patil, P.S. Patil, C.K. Hong, Influence of reduced graphene oxide-TiO<sub>2</sub> composite nanofibers in organic indoline DN350 based dye sensitized solar cells, *Oct. Synth. Met.* 256 (2019) <https://doi.org/10.1016/j.synthmet.2019.116146>.
- [71] C. Jeganathan, T.C. Sabari Girisun, S. Vijaya, S. Anandan, Improved charge collection and photo conversion of bacteriorhodopsin sensitized solar cells coupled with reduced graphene oxide decorated one-dimensional TiO<sub>2</sub> nanorod hybrid photoanodes, *Oct, Electrochim. Acta* 319 (2019) 909–921, <https://doi.org/10.1016/j.electacta.2019.07.036>.
- [72] S.N. Sadikin, M.Y.A. Rahman, A.A. Umar, T.H.T. Aziz, Improvement of dye-sensitized solar cell performance by utilizing graphene-coated TiO<sub>2</sub> films photoanode, *Apr, Superlattice. Microst.* 128 (2019) 92–98, <https://doi.org/10.1016/j.spmi.2019.01.014>.
- [73] S. Pavithra, et al., Photocatalytic and photovoltaic applications of green synthesized titanium oxide (TiO<sub>2</sub>) nanoparticles by *Calotropis gigantea* extract, *J. Alloys Compd.* 960 (Oct) (2023), <https://doi.org/10.1016/j.jallcom.2023.170638>.